Global Evaluation ~~and Application~~ of the Precipitable Water Vapor Product from MERSI-II onboard the Fengyun-3D Satellite

Wengang Zhang[1‡], Ling Wang[2,3‡], Yang Yu[1], Guirong Xu[1], Xiuqing Hu[2,3], Zhikang Fu[1], Chunguang Cui[1]

[1]Hubei Key Laboratory for Heavy Rain Monitoring and Warning Research, Institute of Heavy Rain, China Meteorological Administration, Wuhan 430205, China

[2]Key Laboratory of Radiometric Calibration and Validation for Environmental Satellites, China Meteorological Administration, Beijing 100081, China

[3]National Satellite Meteorological Center, China Meteorological Administration, Beijing 100081, China

Correspondence to: ~~Wengang Zhang~~Ling Wang (~~wengang812~~lingw@~~whihr.com~~cma.cn)

Abstract. The global evaluation of precipitable water vapor (PWV) derived from the advanced Medium Resolution Spectral Imager (MERSI-II) onboard FengYun-3D is performed herein by comparing with the PWV from the Integrated Global Radiosonde Archive (IGRA) based on a total of ~~626~~ 462 sites (~~54214~~ 57,219 match-ups) ~~in total~~ during 2018–~~-~~2021. The monthly averaged PWVs from MERSI-II ~~and IGRA both~~ presents ~~the~~ a decreasing distribution ~~opposite to latitude, with~~of ~~great~~ PWV from ~~mostly found in~~ the tropics to the polar regions. In general, a ~~good~~ sound consistency exists between the PWVs of MERSI-II and IGRA, and their correlation coefficient is 0.~~9400~~ 951 and root mean squared error (RMSE) is 0.~~31~~ 36 cm. The histogram of MB shows that the MB is concentrated around zero and mostly located within the range from -1.00 cm to 0.50 cm. ~~The peak values of mean bias (MB) and the mean relative bias (MRB) are 0.00 cm and -2.38%, with the standard deviations of 0.25 cm and 16.8%, respectively.~~ For most sites, the PWV is underestimated with the MB between -0.~~28~~ 41 cm and 0.05 cm. However, there is also overestimated PWV, which is mostly distributed in the surrounding area~~s~~ of the Black Sea and the middle of South America. ~~The peak values of MB are found in February and July over the Southern and Northern Hemisphere, respectively. More than 66.91% of retrievals falling within the except error (EE) envelope during all months. Overall, the MRB and RMSE become larger with the increasing temporal and distance discrepancy, and it is contrast for EE and correlation coefficient.~~ ~~Besides, the distance discrepancy impacts the evaluation more. The application of PWV product over Qinghai-Tibet Plateau shows that the transport of water vapor along the Brahmaputra Grand Canyon is obvious and it is more significant in July.~~ There is a slight underestimation of MERSI-II PWV for all seasons with the MB value below -0.18 cm, with the bias being the largest magnitude in summer. This is probably due to the presence of thin clouds, which weaken the radiation signal observed by the satellite. We also find that there is a larger bias in the Southern Hemisphere, with a large value and significant variation of PWV. The binned error analysis revealed that the MB and RMSE increased with the increasing value of PWV, but there is an overestimation for PWV smaller than 1.0 cm. In addition, there is a higher MB and RMSE with a larger spatial distance between the footprint of the satellite and the IGRA station, and the RMSE ranged from 0.33 cm to 0.47 cm.

1 Introduction

Water vapor is an important component~~part~~ of the atmosphere and widely known as ~~the most~~an important greenhouse gas ~~and~~ since it can significantly affect climate change, the radiation balance, and the hydrological cycle (Kiehl & Trenberth, 1997; Held & Soden, 2000; Dessler & Wong, 2009; Zhao et al., 2012). The spatiotemporal variations of water vapor are essential for understanding the formation~~s~~ of clouds and mesoscale meteorological systems in that cloud, and precipitation always rely on ~~the~~ changes in~~of~~ water vapor (Trenberth et al., 2003). Furthermore, water vapor can also influence the atmospheric transmittance, and the upward radiance ~~over the view of~~measured by the satellite sensor ~~is also affected by water vapor~~. Therefore, the information of water vapor is highly required to correct atmospheric effects in the satellite-based retrieval algorithm for land surface temperature (Meng et al., 2017).

Considering the critical role of water vapor, technologies aiming at the measurement of atmospheric water vapor have been developed. The precipitable water vapor (PWV), which means the integrated water vapor contained in a vertical column of a cross-sectional area, is an important indicator for the total atmospheric water vapor condition. The two major methods used for measuring PWV are satellite-based and ground-based technologies. Several ground-based measurements, such as radiosonde ~~(~~(Durre et al., 2009~~)~~), global position system (GPS) receivers (Bevis et al., 1992), microwave radiometer (MWR) (Westwater, 1978) and sun photometer (Alexandrovet al., 2009), have been deployed to monitor the variability of water vapor. However, the spatial coverage of ground-based measurements is limited and inhomogeneous, and it is difficult to obtain a wide range of observations from multiple sources to support ~~the~~ studies~~y~~ for the distribution of PWV ~~in~~ on both a regional and global scale~~s~~. This is because the uncertainties ~~in~~ of different measurements are not completely consistent, and they have distinct discrepancies~~, even in the~~ and magnitudes (Chen & Liu, 2016; Wang et al., 2016). Different from ~~the~~ ground-based measurements, the satellite-based measurement is more useful for the temporal analysis of PWV over a wide area. In particular~~Especially~~, the ~~polar~~ polar-orbiting satellite-based measurements of water vapor have ~~the~~ a considerable advantage due to their global coverage with satisfactory temporal and spatial resolutions. Therefore, the ~~polar~~ polar-orbiting satellite-based PWV product is widely used for understanding the global distribution of water vapor. As is commonly known~~As we all know~~, the well knowledge of global water vapor distribution~~s~~ is especially important for global atmospheric models aiming to predict weather or climate. Thus, the water vapor products retrieved via ~~polar~~ polar-orbiting satellites have become essential input parameters to sustain numerical models of the atmosphere, especially where global water vapor information is required within a short time span, and the assimilation of PWV has been ~~proved~~ proven ~~that it can~~to help improve precipitation forecasts (Rakesh et al., 2009).

Over the past few decades, ~~the~~ satellite~~d~~-based PWV retrieval algorithms ~~are~~have been developed with ~~the~~ observations from different sensors, which ~~mainly~~ can be divided into four main types according to the spectral region: (1) visible (VIS), (2) near-infrared (NIR), (3) thermal infrared (TIR), and (4) microwave (MW). There are three major satellite-borne sensors that can provide the global ~~near-infrared (~~NIR~~)~~ PWV product~~s~~. The Moderate Resolution Imaging Spectroradiometer (MODIS) onboard the Terra and Aqua ~~polar~~ polar-orbiting satellite platforms is one of the most important instruments for obtaining global PWV, and ~~it~~ has been widely used for a few decades since the launching of Terra spacecraft in 1999. The Medium Resolution Imaging Spectrometer (MERIS) is one of ten instruments built in Envisat, which was launched on 1 March 2002, but the mission was terminated on 8 April 2012 ~~because of~~due to the loss of contact with the satellite. For the Chinese FengYun 3 (FY-3) meteorological series satellite, one of the major payloads onboard is the Medium Resolution Spectral Imager (MERSI), which primarily monitors the ocean, land, atmosphere, etc. FY-3D is the ~~Chinese~~ second-generation Chinese polar-orbiting meteorological satellite, equipped with the advanced MERSI (MERSI-II), and ~~it is~~was launched on 15 November 2017. For MERIS, the PWV retrieval algorithm ~~employing~~ employ~~ed~~s the ratio of top of atmosphere (TOA) radiance at one water vapor absorption channel (around 900 nm) to the TOA radiance at the atmospheric window channel such as 885 nm~~, which is outside water vapor absorption region~~ (Bennartz and Fischer, 2001). However, both the algorithms for NIR PWV derivation of MODIS and MERSI-II adopt the ~~ratios of~~ reflected solar radiance ratios between three NIR water vapor absorption channels and two non-absorption channels (Gao and Kaufman, 2003; Wang et al., 2021). The setup of non-absorption channels of MERSI-II is the same as that of MERSI but the absorption channels of MERSI-II are similar ~~with~~ to those of MODIS. ~~Besides~~Furthermore, the prelaunch and orbital calibration and characterization of MERSI-II were conducted to ensure the quality of its products (Xu et al., 2018).

It is ~~strongly~~ necessary to evaluate the satellite-based PWV product ahead of its application in atmospheric science research. The PWV from MODIS has been extensively evaluated ~~through~~ by comparing it with the PWV derived from other measurements. The GPS PWV is widely used for the evaluation of PWV derived from MODIS (Liu et al., 2006; Prasad and Singh, 2009; Lu et al., 2011). Ground-based MWR, which can measure integrated water vapor with high temporal resolution and has a reliable measurement under clear sky condition, is also used for the evaluation of MERIS PWV (Li et al., 2003). ~~Additionally~~In addition, the radiosonde PWV, calculated from the integration of specific humidity, has been recognized to be a useful benchmark, being used ~~in~~ for the evaluation of~~g~~ the MODIS PWV in China (Liu et al., 2015), the Iberian Peninsula (Sobrino et al., 2014), and Hong Kong (Liu et al., 2013). However, up to now, few studies have focused on the evaluation of the MERSI-II PWV~~ up to now~~, and the lack of effective assessments greatly limits the application of the MERSI-II PWV product, ~~because~~ since the accuracy of the product ~~cannot~~ has not been fully acknowledged.

Integrated Global Radiosonde Archive (IGRA) is the greatest and most comprehensive collection dataset of historical and near real-time global quality-assured radiosonde observations. It has been used extensively in a variety of studies, including model verification, atmospheric processes, and climate research. Moreover, the radiosonde PWV is also widely applied in the assessments of measurements from other platforms, especially ~~satellite~~ satellite-derived PWV around the world (Adeyemi and Schulz, 2012; Antón et al., 2015; Niilo et al., 2016). Consequently, the IGRA data are selected for the evaluation of the PWV derived from MERSI-II in this study.

The purpose of this paper is to evaluate the MERSI-II PWV globally by comparing it with the global IGRA observations. We are ~~trying~~ seeking to explore the global performance of FY-3D MERSI-II PWV and ~~analyzing~~analy~~s~~z~~ing~~e the influence factors in the evaluation. ~~Besides, the application of MERSI-II PWV on the study for the distribution of PWV over Qinghai-Tibet Plateau (QTP) is also discussed.~~ The structure of this paper is arranged as follows: Data sources and details are discussed in Section 2. Section 3 presents the ~~merging procedures~~ methodology of the merging procedures applied in the sample selection. The evaluation results of MERSI-II PWV against the PWV from IGRA are presented in Section 4. In the final section, ~~A~~a discussion and conclusion of the aforementioned results are given ~~in the final section~~.

2 Data description

The satellite-based PWV product used in this paper is derived from FY-3D MERSI-II, and the ground-based measurements are the PWV data ~~AERONET and IGRA~~ derived from AERONET and IGRA ~~PWV data~~.

2.1 MERSI-II PWV

FY-3D, which was successfully launched on 15 November 2017, is the fourth and latest satellite of the ~~Chinese~~ second-generation Chinese polar-orbiting meteorological satellite. It is operated in a sun-synchronous orbit at an average altitude of 830.73 km, passing over the equator at 13:40 local time (Yang et al., 2019). The MERSI is one of the major instruments carried by FY-3 series satellites, and the MERSI-II onboard FY-3D is an upgraded version of the first-generation instrument. A series of comprehensive prelaunch calibrations have been operated to ensure the high quality of the products from MERSI-II (Xu et al., 2018), which ~~was~~ is from MERSI and has been significantly improved with high-precision on-board calibration and lunar calibration capabilities (Wu et al., 2020). Besides, MERSI-II has 25 channels with a spectral coverage from 0.412 µm to 12.0 µm, and the NIR PWV products of FY-3D are retrieved with three water absorption channels (bands 16, 17, and 18) and two non-absorption channels (bands 15 and 19) in the 0.8–~~-~~1.3 µm range with a spatial resolution of 1 km × 1 km at nadir (Wang et al., 2021). The positions and widths of NIR channels used by MERSI-II and MODIS are given in Table 1. The water vapor absorption channels of MERSI-II, which is now similar ~~with~~ to those of MODIS, are reselected because the three absorption bands have different sensitivities to various water vapor conditions. Therefore, MERSI-II is more useful in the retrieval of water vapor under different conditions (dry, medium, and humid).

Table 1 Characteristics of NIR channels used in PWV retrievals of MERSI-II and MODIS

MERSI-II				MODIS			
Band No.	Position (nm)	Width (nm)	Window channel	Band No.	Position (nm)	Width (nm)	Window channel
15	865	20	yes	2	865	40	yes

16	905	20	no	17	905	30	no
17	936	20	no	18	936	10	no
18	940	50	no	19	940	50	no
19	1030	20	yes	5	1240	20	yes

For the NIR channels, typically with a small aerosol optical thickness that can be ignored, the TOA radiance observed by a downward-looking satellite sensor can be calculated as the following:

$$TOA_{\lambda} = T_{\lambda} \times \rho_{\lambda} , \qquad (1)$$

where TOA_{λ} , T_{λ} and ρ_{λ} are the apparent reflectance, total atmospheric transmittance and surface bidirectional reflectance at the channel with a wavelength of λ, respectively. The term T(λ) contains information of the total amount of water vapor in the Sun–surface–sensor path.

For most types of land surfaces, ~~the~~a reflectance between 850 and 1250 nm changes approximately linearly with the wavelength, therefore, the transmittance of the absorption channel will be calculated by a three-channel ratio of the absorption channel with a combination of two window channels. For the iron-rich soil, the vegetation and snow, although the reflectance does not linearly correlate with the wavelength, ~~the~~ reasonable estimates of water vapor transmittances over these surface types can also be given with the three-channel ratio techniques (Gao and Kaufman, 2003).

By using the MODerate resolution atmospheric TRANsmission (MODTRAN), the transmittances of the five MERSI-II channels as a function of the total water vapor amount under six different atmospheric conditions were calculated, according to the six standard atmospheric models defined in MODTRAN4.3. ~~And~~Furthermore, the results are defined as the transmittance–water vapor lookup table. Based on the solar zenith angle and surface temperature, the atmosphere model can be selected from the six standard atmospheric models, and then the combined two-way water vapor content ~~wa~~is derived using a table-searching procedure. Note that there ~~is~~are no PWV retrievals in the region with a solar zenith angle above 72°, which means the observation time is close to night, due to the weak energy at the satellite's entrance. Subsequently, the derived total water vapor amount will be converted to the vertical column water vapor amount based on the solar and ~~the~~ observational geometries. The ~~A~~absorption coefficients of atmospheric water vapor are very different over the three absorption channels. As a result, the derived water vapor values from the three channels are different even under the same atmospheric condition. In order to solve this problem, a mean water vapor value is obtained from the water vapor values derived from thre~~r~~e absorption channels, by multiplying with the corresponding weight in each channel. A m~~M~~ore detailed description ~~about~~of the algorithm of MERSI-II PWV can be found in Wang et al. (202~~0~~1).

The NIR PWV products derived from MERSI-II have been routinely produced at the National Satellite Meteorological Center, China and can be accessed on the website of http://satellite.nsmc.org.cn/PortalSite/Data/Satellite.aspx. The operational NIR PWV products include the Level-2 5-min granule product and Level-3 global daily, 10-day, and monthly mean products. The Level-2 products are generated on a pixel-by-pixel basis (i.e., 1 km × 1 km) from standard MERSI-II L1B radiance datasets as well as ancillary data from the L1B geolocation and the cloud mask (CLM) product of MERSI-II. The outputs from the Level 2 product include the total weighted column water vapor amount on a pixel-by-pixel basis, independently derived PWV from one of the water vapor absorption channels, and an associated quality assurance parameter that indicates whether the inversion algorithm has a two-channel or three-channel ratio and whether a pixel is clear or ~~As we all know, the NIR PWV product from MERSI-II is the total column amount of water vapor over cloudless land of the globe as well as above clouds. Besides, over the oceanic areas with sun glint the PWV product can also be obtained. However, in order to consist with the ground-based measurements, only the~~cloudy. The Level-2 5-min granule PWV product ~~over cloudless land area~~ is ~~used~~ evaluated in this study~~.~~, and ~~The~~the data span is from September 2018 to June 2021 with a spatial resolution of 1 km × 1 km.

2.2 Radiosonde

The Integrated Global Radiosonde Archive (IGRA), which is a collection of historical and near real-time global radiosonde observations, is archived and distributed by the National Centers for Environmental Information (NCEI), formerly known as the National Climatic Data Center (NCDC), and ~~it~~ can be accessed at ftp://ftp.ncdc.noaa.gov/pub/data/igra. Version 2 of IGRA (IGRA 2) is used in this study. A total of 33 data sources, including 10 out of 11 source datasets used in IGRA 1, have been integrated into IGRA 2, which was fully operational on August 15, 2016, and has a higher spatial and temporal coverage. Therefore, compared to IGRA 1, the IGRA 2 contains nearly twice as many sounding stations and 30% more soundings. Sounding-derived parameters are recorded according to separated station files and continue to be updated daily, and PWV is one of the derived parameters. PWV will be calculated if the pressure, temperature, and dew point depression are available from the surface to a~~the~~ level of 500 hPa (Durre et al., 2009). The calculation involves the acquirement of specific humidity at each observation level and then the integration of specific humidity between the surface and the level of 500 hPa, so that IGRA-derived PWV is recognized as surface-to-500-hPa PWV. As discussed by Turner et al. (2003), the PWV obtained from radiosonde has an approximate 5% dry bias compared to that derived from the MWR. Therefore, there is an underestimation of PWV evaluation for taking the IGRA-derived PWV as a reference, and the bias found in the tropical area~~s~~ is ~9% (Zhang et al. 2018). Due to the time range of IGRA data, there are only ~~625~~ 462 out of 1535 global IGRA stations that can be matched with the FY-3D MERSI-II PWV products.

2.3 AERONET

The federated Aerosol Robotic Network (AERONET) is a network of ground-based Cimel Electronique Sun photometry, which can measure beam irradiance and directional sky radiance routinely during the daytime in clear conditions (Holben et al., 1998). AERONET was established by NASA and PHOTONS (PHOtométrie pour le Traitement Opérationnel de Normalisation Satellitaire), primarily aiming to provide public domain dataset of global aerosol optical and microphysical properties. In addition, based on the measurements at the 940 nm water-vapor channel and the atmospheric window bands centered at 870 nm and 1020 nm, PWV was also calculated (Che et al., 2016). The AERONET version 3 database provides three levels of data: Level 1.0 (unscreened), Level 1.5 (cloud-screened), and Level 2.0 (cloud-screened and quality-assured), and ~~it~~ can be accessed at https://aeronet.gsfc.nasa.gov. Level 2.0 dataset, which is used in this study, signifies an automatically cloud-cleared, manually quality-controlled dataset with pre- and post-field calibrations applied. All the instruments in the AERONET are annually calibrated with reference to the world standard: the Mauna Loa Observatory (Malderen et al., 2014). Thus, the measuring accuracies of different AERONET stations are accurate and consistent (Liu et al., 2013). As discussed by Pérez-Ramírez et al. (2014), PWV obtained from AERONET has a dry bias of approximately 0.16 cm against the radiosonde PWV and it is reasonable for ~~the~~ meteorological studies.

3 Methodology

3.1 Statistical indicators

The common statistical indicators, such as the mean bias (MB, perfect value = 0), the mean relative bias (MRB, perfect value = 0), correlation coefficient (CC, perfect value = 1) and the root mean squared error (RMSE, perfect value = 0), are used to evaluate the precision of the retrieved PWV from MERSI-II. ~~The MB, which can indicate the tendency of underestimation or overestimation, is desirable to be close to zero. The MRB can be defined as the percentage deviation between the derived and observed PWVs, and its perfect value is 0. CC is an indicator that can quantify the agreement between PWVs of MERSI-II and IGRA, and the closer of the CC to 1 means a better coherence. The RMSE reflects the actual deviations between the paired derived value and reference value, and lower RMSE values are preferred with a perfect value of 0. Besides, we adopt the percentage of matching data falling within an expected error (EE) envelope and it is expressed as EE value in this paper. EE envelope is popularly used in the evaluation of aerosol retrievals, and an EE value of >66% indicates satisfactory agreement (Levy et al., 2010). In addition, the EE envelope defined as ±15% is also used in the validation analysis of MODIS derived PWV product the same (Martins et al., 2019).~~ All ~~the~~ calculations of indicators are presented as follows:

$$MB = \frac{1}{N}\sum_{i=1}^{N}(PWV_{si} - PWV_{gi}) \ ,$$

(~~1~~2)

$$MRB = \frac{1}{N}\sum_{i=1}^{N}(\frac{PWV_{si} - PWV_{gi}}{PWV_{gi}}) \times 100\% \ ,$$

(~~2~~3)

$$CC = \frac{\sum_{i=1}^{N}(PWV_{si} - \overline{PWV_{si}})(PWV_{gi} - \overline{PWV_{gi}})}{\sqrt{\sum_{i=1}^{N}(PWV_{si} - \overline{PWV_{si}})^2 \sum_{i=1}^{N}(PWV_{gi} - \overline{PWV_{gi}})}} \ ,$$

(~~3~~4)

$$RMSE = \sqrt{\frac{1}{N}\sum_{i=1}^{N}(PWV_{si} - PWV_{gi})^2} \qquad (\cancel{4}5)$$

~~$EE = \pm(0.05 + 0.15 \times PWV_g)$ (5)~~

where PWV_s is the MERSI-II PWV product, PWV_g is the IGRA PWV product, and N is the total number of match-up.

3.2 Collocation strategy

As we have mentioned above, FY-3D is ~~primary~~ operated in a ~~sun~~Sun-synchronous orbit with an equator crossing time at 13:40 local time. However, the radiosonde is released at 00:00 UTC and 12:00 UTC and there is a significant temporal discrepancy between satellite and radiosonde at most sites. ~~Besides~~Furthermore, the distribution of radiosonde site is sparse over the globe. For the evaluation of PWV from global reanalysis models with a temporal resolution of 6 h, temporal window of ± 3 h and distance of ± 50 km is employed in the comparison with PWV from Maritime Aerosol Network (Pérez-Ramírez et al., 2019).

In order to determine the temporal collocation window that can adequately match the satellite observations with the ground-based measurements, the ~~consistency~~ consistencies between the existing AERONET PWV and the temporal averaged AERONET PWV ~~measurements~~ in various temporal discrepancy intervals from 1 h to 6 h with a step of 1 h, that is, 0–1 h, 1–2 h, ~~and so on~~etc., ~~is~~ are ~~analyzed~~analy~~s~~zed respectively. In processing, only the existing AERONET PWV~~point~~, which~~that~~ has the matching ~~data~~ averaged AERONET PWV in each temporal discrepancy interval, is selected for the ~~comparison reliability~~determination of the temporal collocation window. Therefore, there is the same number of collocations for all the temporal discrepancy intervals. The results are presented in Figure 1, and ~~obviously~~as evidenced, there is a good consistency ~~at~~ in all situations with the CC larger than 0.969~~0~~ and the slope ~~is~~ larger than 0.965. Although MRB and RMSE become larger with the increasing temporal interval, their values are less than 1.7~~0~~% and 0.23 cm, respectively. Moreover, it can be observed that the MB values of all comparisons are 0.00 cm, which suggest~~s~~ that the biases are~~is~~ distributed equally around zero. ~~More than 80.92% match points are within the EE and the largest value is 99.97% when the temporal discrepancy is within 1 h.~~ Therefore, we ~~make the conclusion~~ conclude that the temporal collocation window for PWV evaluation can be set to 6 h.

PWV-AERONET(cm)

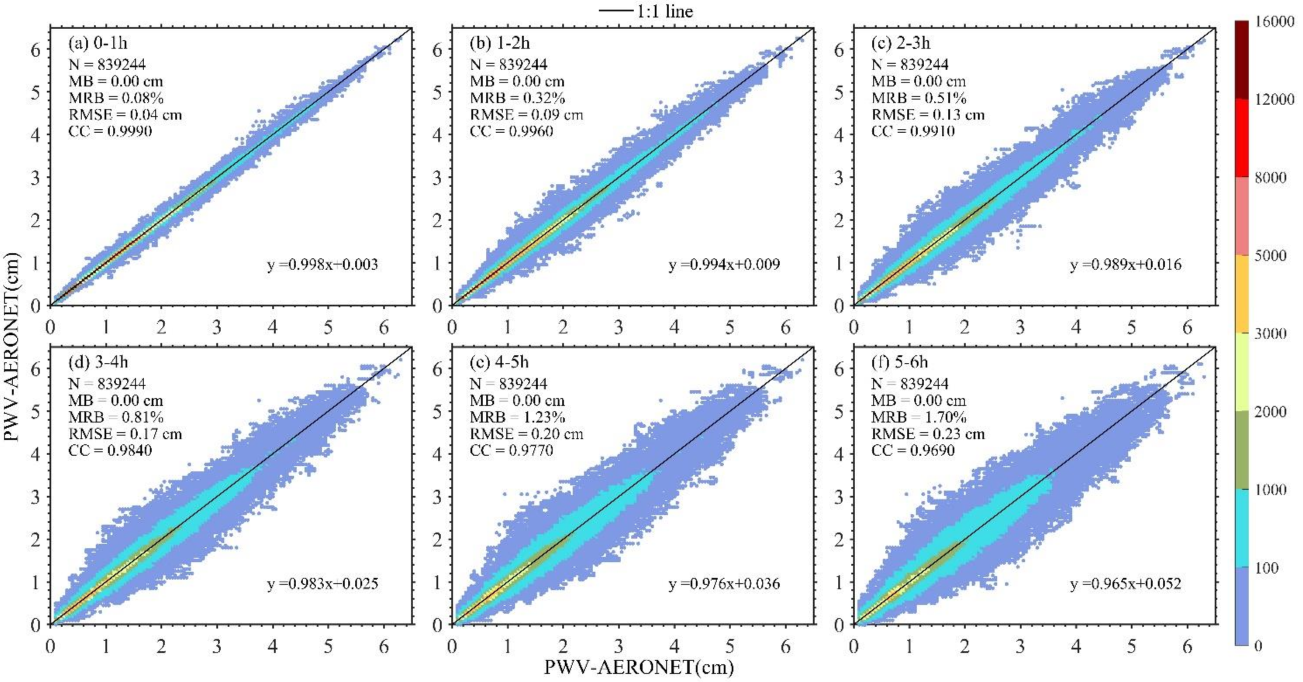

Figure 1 Scatter plots of PWV derived from AERONET in different temporal discrepancy intervals and (a)–~~-~~(f) present the temporal discrepancy of 0–~~-~~1 h, 1–~~-~~2 h, 2–~~-~~3 h, 3–~~-~~4 h, 4–~~-~~5 h and 5–~~-~~6 h, respectively. The solid line represents the ~~line~~ 1:1 line~~, dashed lines are the envelope lines of EE~~. The color~~-~~bar depicts the number density of match-ups for each bin of PWV in a 0.01 cm×0.01 cm grid. ~~Proportion of matching data falling into EE envelope is presented by −EE value.~~

For the MERSI-II, the spatial resolution at nadir is 1 km ×~~×~~ 1 km for NIR bands, which are used for the retrieval of PWV. It is not perfectly justifiable that the PWV in an image pixel represents the surrounding averaged PWV (Ichoku et al., 2002), and during the ascending of balloon, its lateral drift should also be considered. Therefore, ~~we use the standard deviation (STD)~~the spatial averaged PWV ~~of~~ within a box ~~with~~ of 9×9 pixels ~~to eliminate the invalid PWV measurement~~was calculated. Furthermore, only when all pixels within the box ~~we~~are confidently proved to be clear by the MERSI-II CLM product, the pixel is marked as reliable and the PWV of the central pixel is replaced by the spatially averaged PWV value. ~~In operation, we set a general principle that the STD of this selected box must be less than 0.25 cm and the value of the STD dividing the minimum within the selected box must be less than 1.~~ Otherwise, the ~~data~~ pixel is marked as unreliable and will not be selected for the comparison. ~~This is because the PWV in clear sky is considered as less varied in a local area based on the analysis of PWV derived from AERONET. In addition, the cloud mask (CLM) product of MERSI-II is applied in the collection of comparison samples of MERSI-II PWV and radiosonde PWV. For the MERSI-II CLM product, there are four clear-sky confidence levels (confidently clear, probably clear, probably cloudy, cloudy) for each pixel and they are denoted by the values of 3, 2, 1, and 0, respectively. Only the situation in which all pixels of the selected box are confidently clear is considered and~~

~~collected for MERSI-II PWV product.~~ Unfortunately, there is no cloud measurement in the radiosonde observation, so the cloud detection method with the relative humidity threshold of sounding is employed here (Zhang, 2010), and then the cloudless radiosonde PWV dataset is established.

In this study, the threshold of the horizontal distance between an IGRA station and the footprint of MERSI-II is set to be 50 km (Qin et al., 2012; Pérez-Ramírez et al., 2019). In processing, all the reliable PWV retrievals derived from MERSI-II within ±6 h of the radiosonde release time are ~~all~~ collected and only the spatial closest PWV retrieval ~~of MERSI-II~~ within ~~100~~ a 50 km distance~~d~~ from the IGRA site is selected and matched ~~up~~ with the IGRA-derived PWV. Figure 2 illustrates the available sample numbers of radiosonde sites over the globe ~~during~~ from 2018–~~-~~2021, with a ~~totally~~ total of ~~626~~ 462 sites. The sample numbers of all sites vary from 15 to ~~474~~418, and observations are concentrated in the Northern Hemisphere. Around the equator, few samples are ~~got~~ obtained due to the high occurrence frequency of clouds and precipitation. Most frequently sampled places are China, Europe, and ~~northern~~ North America, where IGRA sites are densely distributed, while there are few match-ups in Africa ~~because~~ since radiosonde stations associated with IGRA in this region are sparse~~rarely seen there~~ (Durre et al., 2018).

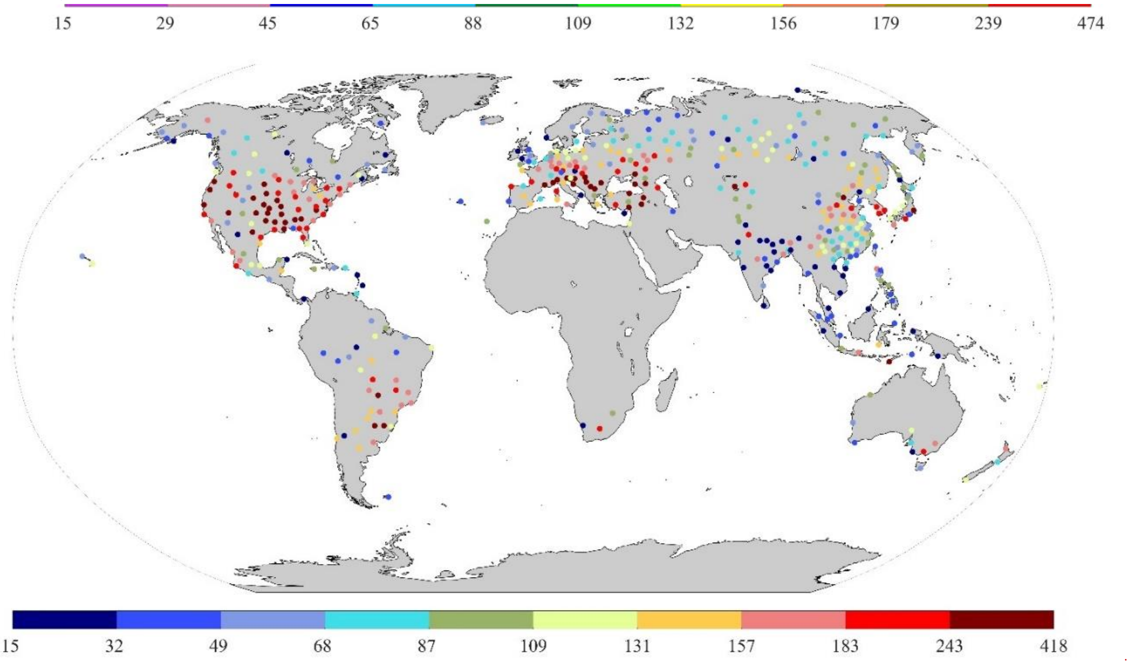

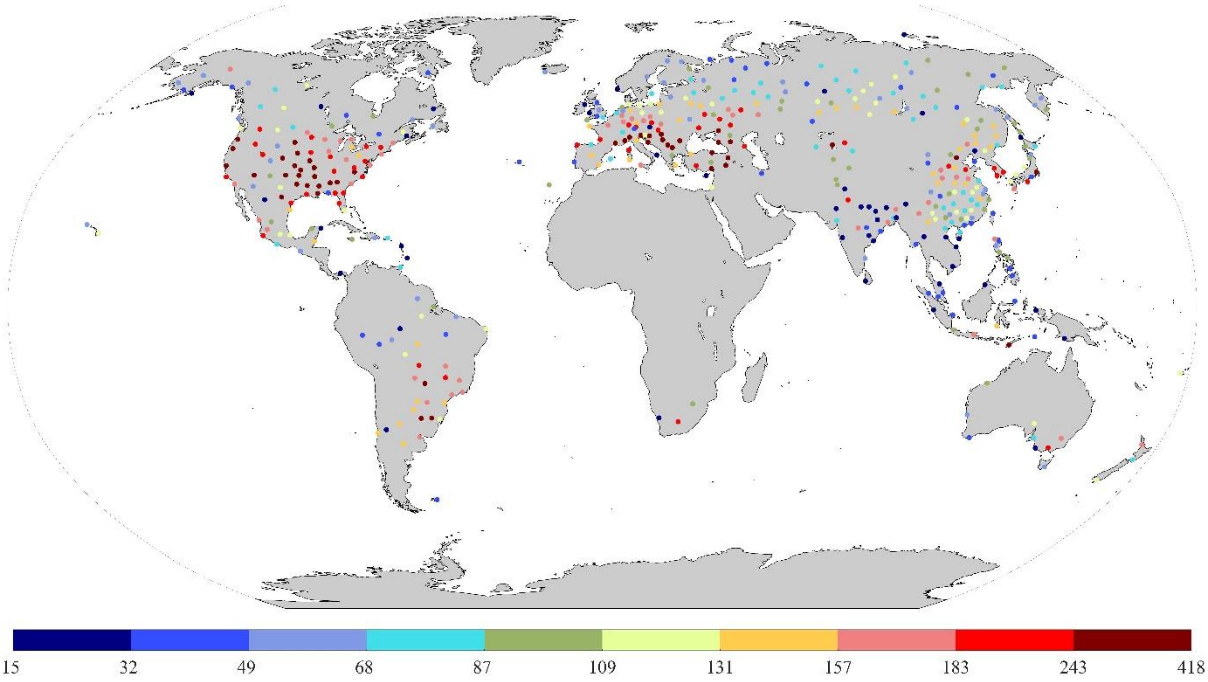

Figure 2 Number of matchups between MERSI-II and IGRA PWV observations for each site ~~during~~ from 2018~~-~~–2021.

4 Results and Discussion

4.1 Global ~~comparison~~evaluation of PWV derived from MERSI-II

Figure 3 illustrates the global monthly averaged PWV obtained from the MERSI-II~~ and IGRA under clear sky conditions.~~ for the month of July in 2020. In general, ~~both~~ the averaged PWV derived from MERSI-II~~ and IGRA~~ shows ~~the~~ a decreasing distribution of ~~decreasing value~~PWV with ~~the~~ increasing~~opposite to~~ latitude, ~~with~~ and large PWV values are mostly found in the tropics but rare in high latitudes. High PWV values (> 3.0 cm) are mostly detected in the Amazon rainforest of South America, ~~East~~West and South Asia, southeastern China, Southeast Asian islands, and central Africa. The significantly high PWV center in West Asia is mainly contributed by the Indian moon during the summer season. The PWV contents over the Qinghai~~-~~–Tibet Plateau and Greenland are small because of the high altitude and high latitude, respectively. Furthermore, due to the winter season of July in the Southern Hemisphere, small PWV contents are also presented over the southern parts of South America and Africa, as well as Australia. ~~Around the tropics with latitude between 20°S and 20°N, the greatest PWV values are found with most PWV values above 2.17 cm. Lower PWV values are presented in mid-latitude, but the variability of PWV is the largest here with the values range from 0.60 cm to 2.17 cm. The PWV values in high latitudes are the lowest~~

~~and most sites have the PWV values below 1.44 cm. The global distribution of averaged PWV is uneven and generally characterized by one low and two high PWV centers. The low center is in the east of Russia and the northeast of China, with PWV below 1.16 cm measured at most sites. The two high centers are in the surrounding areas of the Bay of Bengal and the middle part of South America, with most PWV values larger than 1.72 cm.~~

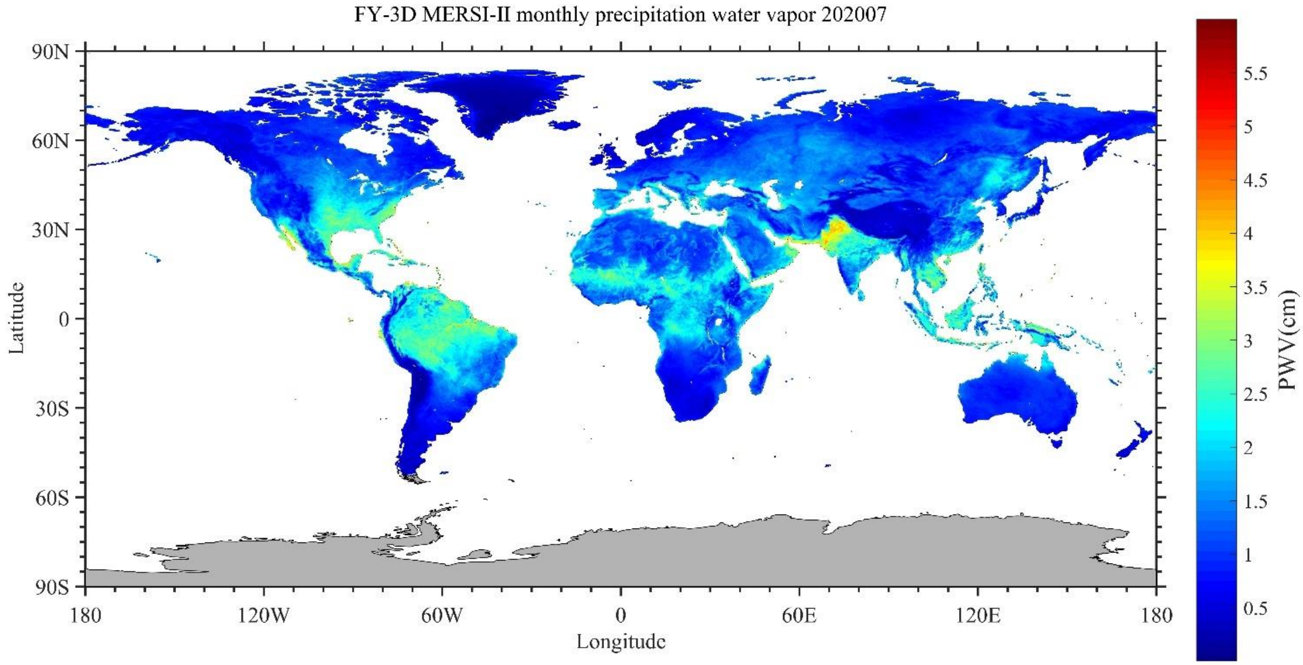

Figure 3 Global averaged Level-3 NIR precipitable water vapor (PWV) image derived from FY3D MERSI-II in July 2020~~.~~ ~~Global averages of PWV derived from MERSI-II (a) and IGRA (b) for each site~~.

Figure 4a shows the scatter plot~~s~~ of PWV derived from MERSI-II against IGRA observations. There are ~~54214~~ 57,219 match-ups in total and the MERSI-II (IGRA) PWV ranges from 0.11(0.05) cm to ~~4~~6.07 (~~5~~6.~~9~~78) cm, with a high number density between 0.20 cm and 2.00 cm. Moreover, ~~I~~it is found that the MERSI-II and IGRA PWV measurements are well correlated with CC of 0.~~9400~~951, while the retrieved PWV from MERSI-II is slightly underestimated, with an MB of -0.~~09~~ 1~~2~~1 cm and an MRB of -~~1.90~~2.2%. ~~Besides~~Furthermore, the RMSE is 0.~~31~~ 36 cm ~~and the EE value is satisfactory (75.36%),~~ and the statistical biases are slightly larger than those from the evaluation of MODIS over globe by comparing with the observations of AERONET (Martins et al., 2019). It is ~~considerable~~ considered that the satellite has a larger temporal discrepancy with radiosonde than AERONET, which has a high temporal resolution of about 1 min, and from the discussion in section 3.2, ~~the~~a large temporal discrepancy~~this~~ will ~~also~~ cause ~~the~~ an increasing ~~error~~bias in the evaluation of the ~~MERSI-II~~ PWV product. ~~Although the reasonable MB and MRB have been found in the evaluation of all sites, there are some individual points with the unnormal MB and MRB. Therefore, the top 1% and bottom 1% of MB and MRB are not present in the histogram in order to show an intuitive acknowledge of distributions of MB and MRB.~~ Figure 4b reveals the distribution of MB between FY-3D MERSI-II and IGRA with a bin widt**h of 0.05 cm**, and notably, the MB is concentrated around zero and there is a small flattening towards negative values~~the bias distribution is left-skewed, which means that there are more negative MB values~~. ~~.~~ ~~However~~ Moreover~~Besides~~, ~~the peak value of MB is 0.00 cm and~~ there are ~~23~~20.8% of all points within the interval from -0.05 cm to 0.05 cm, and the standard deviation (STD) of MB is 0.~~25~~ 34 cm. It can be concluded that there is ~~a~~ high accuracy for the MERSI-II PWV product, as evidenced by the low MB and STD which are similar ~~with~~ to those in the evaluation of ground-based GPS PWV against radiosonde PWV (Wang et al., 2007). Although the MB is mainly distributed between -1.00 cm and 0.50 cm, it is observed that there are also some points with a large MB value. As presented in figure 4b, the large MB is mostly with a negative value, and this is mainly due to the different situations observed by the radiosonde and satellite because of the radiosonde drift and the large temporal discrepancy between MERSI-II and IGRA observations. Due to the lack of cloud measurement in the radiosonde observation, the PWV from IGRA possibly contains the point ~~that~~ in ~~the~~ cloudy conditions, which is proved to hav~~eing~~ a larger water content than clear conditions (Zhang et al., 2015). For ~~the~~ most ~~of~~ large positive MRB, there is a large temporal discrepancy of more than 4 h, and this ~~can be~~is recognized as the primary reason for the high positive MRB. ~~For the MRB shown in Figure 4c, the distribution is also centered around zero but with a right-skewed pattern, and the peak value of MRB is -2.38% with the STD of 16.8%. The highest frequency of interval ranges from -4.0% to -2.0%, with more than 5.9% of all retrievals falling within this interval. And this result is comparable to the accuracy of MODIS NIR PWV product, which is compared with MWR PWV and with a 5%-10% error range (Gao & Kaufman, 2003). Besides, the analysis and explorations of high MB and MRB values indicate that the dominant large values of MB and MRB are caused by the matchups with high temporal discrepancy or large distance between FY-3D and IGRA observations.~~

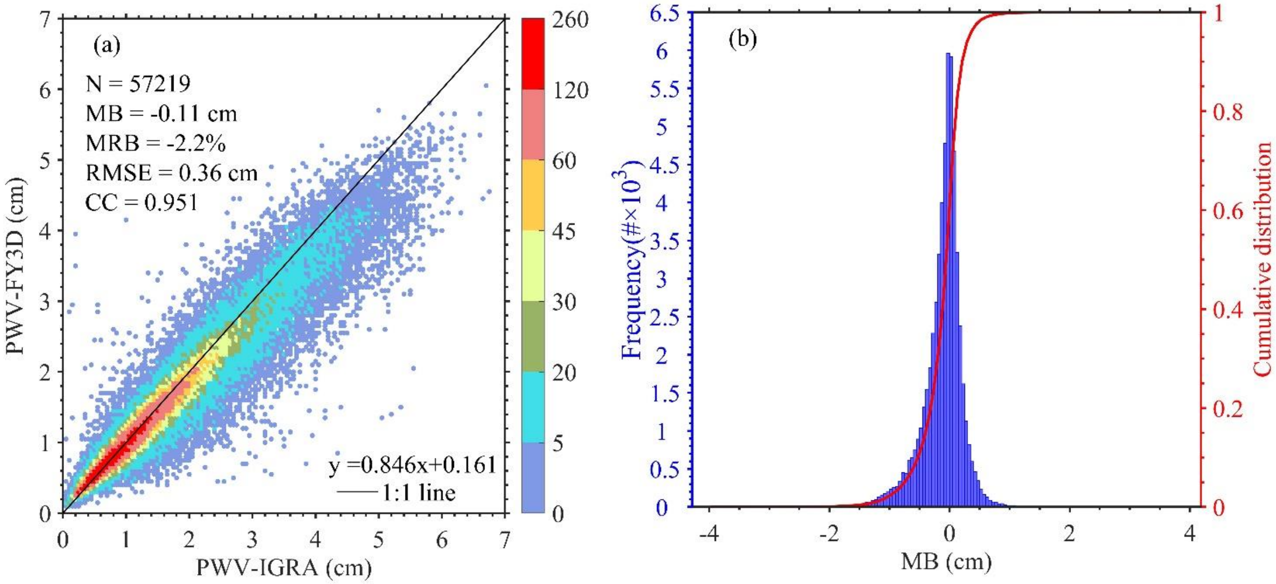

Figure 4 (a) Total density scatterplot of the PWV derived from MERSI-II against that of IGRA ~~for all sites~~for each bin of PWV in a 0.05 cm×0.05 cm grid. The solid line represents the 1:1line ~~1:1~~. (b) Frequency histogram~~s~~ of ~~(b)~~ MB ~~and (c) MRB~~ between MERSI-II and IGRA PWV superimposed on a cumulative distribution curve.

4.2 Evaluation of MERSI-II PWV product in different locations

Figure 5 shows the geographical distributions of PWV comparison statistics of 462 sites between MERSI-II and IGRA over the globe. In order to equally present the statistical indicators, all sites are ~~approximately~~ separated into approximately ten equal parts, that is, the site number of each part is ~43. Consequently, the steps of comparison statistics are not equidistant in the presentation. As we can see from the MB distribution in Figure 5a, the MB mostly presents a low value~~s~~ between -0.~~28~~ 41 cm and 0.05 cm~~ at 80% of the sites~~. About 80% of all sites have negative MB values, and this indicates that PWVs derived from MERSI-II are primarily underestimated compared with IGRA PWV values. ~~There are 10% of all m~~Most sites with ~~larger~~ an ~~high~~ MB value~~s~~ larger than -0.~~28~~ 41 cm~~, and most sites~~ are distributed in the west and south of Asia, with a large mean PWV content but a small number of match-ups. ~~Besides~~Furthermore, attributed to the monsoon climate, there is a large seasonal variation over this region, particularly in the south foothill of the Himalayas (Chen and Liu, 2016). Those sites with overestimated PWV values of MERSI-II are mostly distributed in the surrounding areas of the Black Sea and ~~the~~ central South America, and most of them have ~~the~~ MB values larger than 0.05 cm. It is also found in the evaluation of the PWV product derived from MODIS onboard Terra ~~and Aqua, and~~ that the MB of MERSI-II is slightly smaller~~, especially compared with that of Terra~~ (Martins et al., 2019). In general, the distribution of the MRB (Figure 5b) is similar ~~with~~ to that of the MB at most sites. However, there are two areas that have slight discrepancies between them. One area is in eastern Russia and northeastern China, where there are some sites with ~~the ~~a large~~r~~ MRB value~~s~~ above ~~4.45~~3.3%, although with ~~the ~~a small MB value~~s~~ ~~are small over this aera with the values range ~~ranging from -0.~~08 ~~10 cm to 0.05 cm. As we can see from figure 3, there is a low averaged PWV value in this region, and this is the dominant reason for the great MRB values but with small MB values over this a~~e~~rea. Another area is ~~the middle part of~~central South America, where the sites have large MB values and comparatively low MRB values, and this is because of the large mean PWV values in this region. The larger evaluation ~~error ~~bias of PWV~~s~~ derived from MODIS and reanalysis products has also ~~have had ~~been found in the middle of South America, with most sites ~~have ~~ha~~d~~ving the MB and RMSE both larger than 0.40 cm (Lu, 2019; Wang et al., 2020). Figure 4c depicts the distributions of RMSE for all sites and most sites have a small RMSE ~~present low values with 90% of sites ~~below 0.~~49 ~~48 cm. The large RMSE values are primarily found at low latitudes, mostly in South and Southeast Asia. However, in the east of Europe, there are small RMSE with values below 0.~~21 ~~2~~3~~1 cm at most sites. In general, there is a good agreement between MERSI-II and IGRA PWV at most sites with the CC value above 0.~~8782~~873. The highly correlated sites are mainly distributed around the east of Europe and have ~~the ~~CC values larger than 0.~~9557~~958, while ~~the ~~low CC values ~~that ~~smaller than 0.~~8213 ~~814 are predominantly concentrated around the equator. There are large biases but small CC values over the equator, and ~~it~~that is possibly~~e~~ due to the following: 1) large residual IGRA PWV above 500 hPa (Boukabara et al., 2010); 2) high content and variation of PWV (Chen and Liu, 2016); 3) the covered surface with the reflectance does not linearly correlate with the wavelength (Gao and Kaufman, 2003); ~~and ~~4) a small number of samples. In addition, the temporal discrepancy can also lead to ~~the ~~bias because the discrepancy in the equatorial region is slightly larger than in other regions overall. As discussed by Alraddawi et al (2018), for MODIS PWV, there are also noteworthy latitudinal decreases for MB, MRB and RMSE.

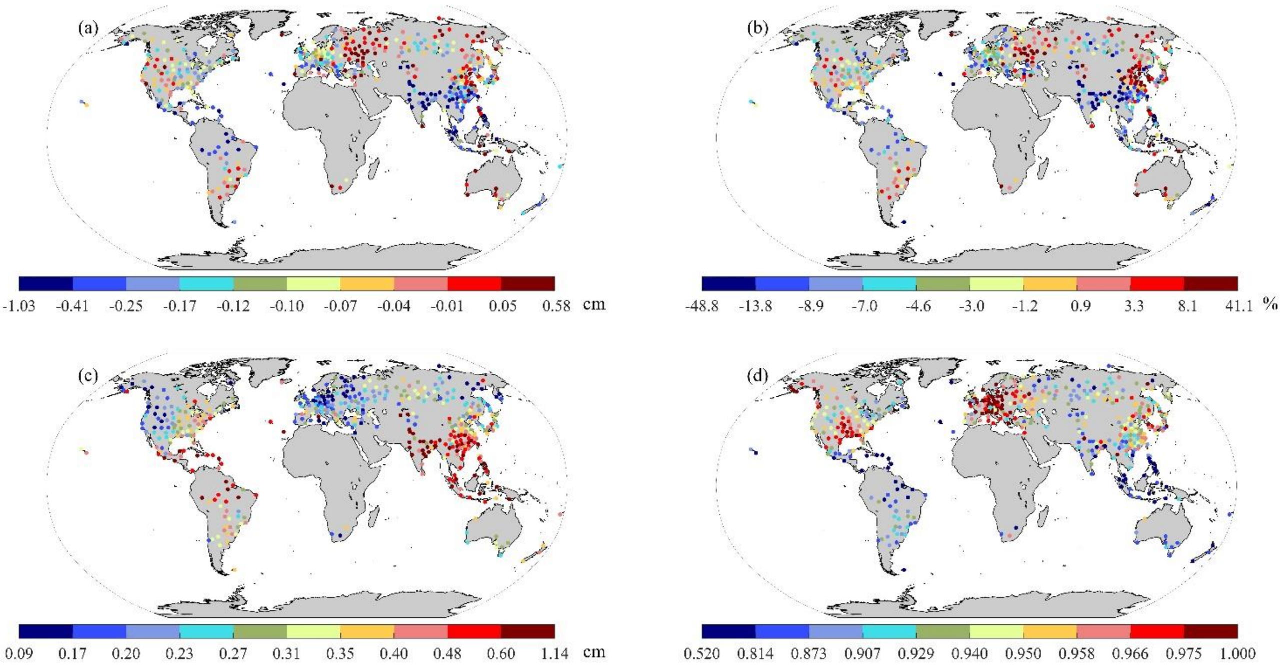

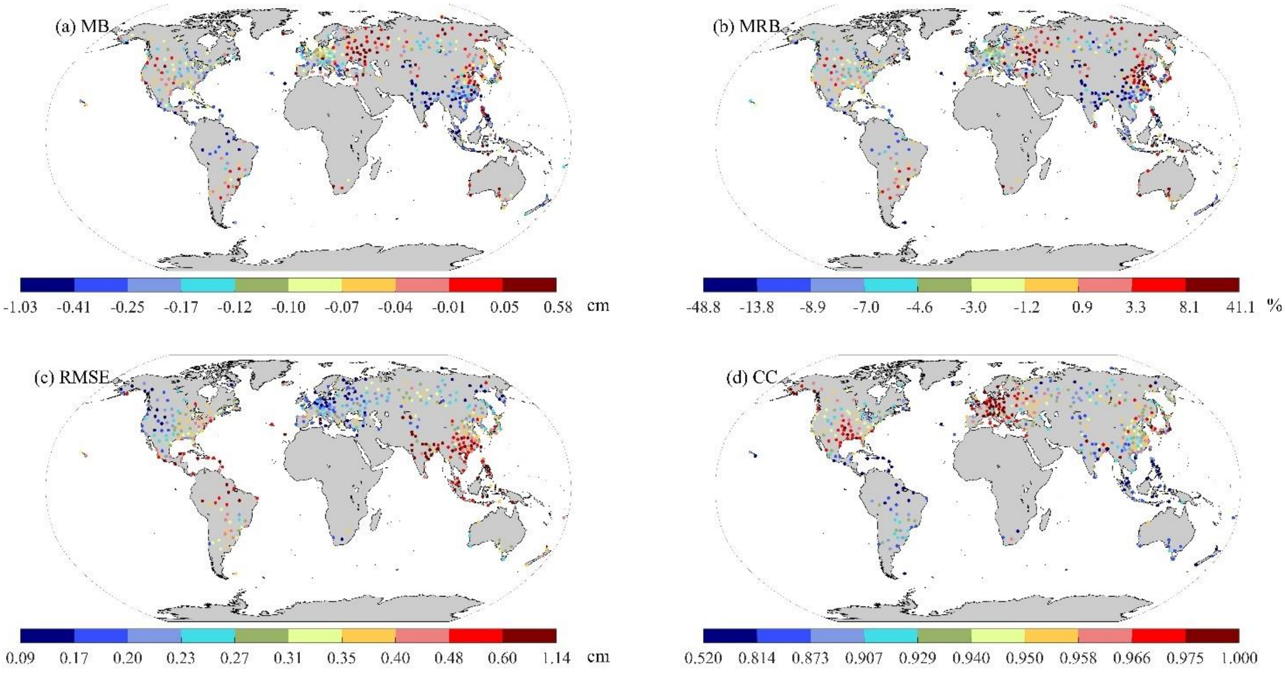

Figure 5 The geographical distributions of PWV comparison statistics between MERSI-II and IGRA. (a) MB; (b) MRB; (c) RMSE; (d) CC.

4.~~2~~ 3 The annual performance of MERSI-II PWV product~~emporal variations analysis~~

As we ~~have~~ mentioned above, PWV presents a notable temporal variation~~,~~. ~~and the seasonal variation is a key point to characterize the climatic change of PWV.~~ Therefore, ~~a seasonal comparison between the PWVs derived from MERSI-II and IGRA is firstly analyzed in this section~~the annual performance of the MERSI-II PWV product by season ~~i~~was evaluated and the results are given in Table 2. It is noted that the number of samples in each season is significantly different.

Table ~~1~~ 2 Seasonal~~Monthly~~ statistics of comparison between PWVs derived from MERSI-II and IGRA in the Northern (Southern) Hemisphere

Season	N	Slope	MB (cm)	MRB (%)	RMSE (cm)	CC
MAM	11866(1232)	0.833(0.859)	-0.09(-0.10)	-1.8(-1.4)	0.31(0.39)	0.954(0.953)
JJA	15935(2187)	0.807(0.873)	-0.18(-0.05)	-5.3(1.7)	0.41(0.34)	0.931(0.953)
SON	16196(2176)	0.836(0.858)	-0.11(-0.06)	-2.5(0.3)	0.34(0.41)	0.945(0.933)
DJF	6558(1069)	0.852(0.799)	-0.05(-0.17)	3.8(-3.9)	0.31(0.49)	0.944(0.921)

The number of match-ups ranges from 6558 (1069) to 16196 (2187) in the Northern (Southern) Hemisphere for all seasons. In all seasons, the slope values are all less than 0.873, which is the fit-slope in winter in the Southern Hemisphere. The MERSI-II PWV is underestimated for all seasons, and the MB is less than -0.18 cm. The MB is obviously large in the warm season, and it is more significant during the summer. With abundant water vapor in summer, clouds are easily to form, however, thin clouds are difficult to be measured by satellite due to their low optical depth (Solbrig, 2009; Naumann and Kiemle, 2020). Therefore, the higher underestimation of PWV in summer is probably triggered by the weakened or covered radiation signal under the thin cloud. For MRB, the variation is within a large range, and the largest MRB is in summer ~~both~~ over both the Northern and Southern Hemisphere, with values ~~being~~of -5.3% and -3.9%, respectively. For the largest MRB during winter in the Northern Hemisphere, ~~it is~~this m~~ay~~ight be related to the points with a small PWV value but a high positive MB, because we firstly calculate the MRB for each match-up and then average all MRB values in seasons. In addition, MRB is mostly negative during the warm season, but positive in the cold season. The RMSE in the Northern Hemisphere is slightly smaller than that in the Southern Hemisphere, where the greatest RMSE value is 0.49 cm in summer. There is a large oceanic coverage in the Southern Hemisphere, with ~~the~~a larger mean PWV than that in the Northern Hemisphere (Chen and Liu, 2016). Thus, ~~it~~this is a~~the~~ possible reason accounting for large RMSE in the Southern Hemisphere, ~~in consideration of~~considering the increasing bias of the remote sensing PWV with the larger PWV value. ~~Besides~~Moreover, there is ~~a better~~ an improved correlation between PWV derived from MERSI-II and IGRA, and all CC values are larger than 0.921.

~~Figure 6. The four seasons in the Northern Hemisphere are defined as follows: spring (MAM), summer (JJA), autumn (SON) and winter (DJF), and it is opposite in the Southern Hemisphere. There are slight underestimations of MERSI-II derived PWV for all the four seasons. The MBs in summer and autumn are both large with the magnitude greater than 0.09 cm but~~

~~with negative values, and the MB value is larger in summer. With abundant water vapor in summer, clouds easily form, however, thin clouds are difficult to be measured by satellite due to their low optical depth (Solbrig, 2009; Naumann and Kiemle, 2020). Therefore, the higher underestimation of PWV in summer is probably triggered by the weakened or covered radiation signal under the thin cloud. The RMSE is within 0.35 cm in all the four seasons, especially in winter when the RMSE is 0.27 cm and MB is at the value of -0.04 cm. Besides, the MRB also presents the similar seasonal variations, with a peak value in summer and a minimum value in spring. The MRB is positive in winter, and this may be related to the small PWVs with a high positive MB in winter. Moreover, the PWV derived from MERSI-II has strong correlations with IGRA PWV and the CC is larger than 0.9080 in all seasons. However, the EE values, ranging between 73.10% (winter) and 77.47% (summer), do not show obvious seasonal variations.~~

~~Figure 6 Seasonal scatterplots for the PWV comparison between MERSI-II and IGRA in (a) spring, (b) summer, (c) autumn and (d) winter.~~

~~In addition, the monthly performance of the MERSI-II PWV product is also evaluated. Table 1 demonstrates the results compared with PWV of IGRA. The number of match-ups ranges from 1847 (224) to 5956 (742) in the Northern (Southern) Hemisphere. The MERSI-II PWV is underestimated in all months, and the underestimation is more significant in the Northern Hemisphere. The slope values are less than 0.832, which is the fit-slope in March. However, the fit-slope in the Southern Hemisphere is greater than 0.801 except in January and February, and the greatest and smallest values are 0.874 (June) and 0.754 (February). Most of MB values are less than 0.10 cm and the peak MB values mainly appear in February in the Southern Hemisphere and July in the Northern Hemisphere. For MRB, the variation is within a large range, and the largest MRBs are in June and July over the Southern and Northern Hemispheres, with values being 4.06% and -5.43%, respectively. During warm seasons, MRB is negative in most cases, but positive in cold seasons. The RMSE in the Northern Hemisphere is slightly smaller than that in the Southern Hemisphere, where the greatest RMSE value is 0.40 cm in December. Besides, there is a better correlation between PWVs derived from MERSI-II and IGRA in the Northern Hemisphere, and all CC values are larger than 0.9070 except in July. The percentages of within EE envelope lines are all larger than 66%, which is the threshold value of satisfactory consistency.~~

4.~~3~~ 4 ~~The influence~~ Influencing factors on evaluation

As ~~we~~ mentioned above, there is a higher bias with the larger PWV value, and this is found in the evaluation of MODIS PWV product (Martins et al., 2019). ~~Besides~~Furthermore, the impact of the spatial distance between the footprint of the satellite and the IGRA station on the evaluation of PWV is also considered in the validati~~ng~~on of HY-2A CMR PWV (Wu et al., 2020b). In this section, ~~the~~ influenceing factors~~,~~ such as the value of IGRA PWV~~,~~ and the spatial distance between the footprint of the satellite and the IGRA station, are all explored in order to quantify their effects on the evaluation of MERSI-II PWV. ~~s with different temporal and distance intervals are compared with the IGRA PWV in order to explore the effects of dissimilar discrepancies of time and distance on the evaluation of MERSI-II PWV. Furthermore, the altitude difference has an important influence on the accuracy evaluation of PWV, so we also present the deviation of MERSI-II PWV for each class of station altitude. Besides, the statistics in different latitudes is presented for analyzing the accuracy of MERSI-II PWV over different regions.~~ Table 3 illustrates the evaluation results of the MERSI-II PWV in different intervals of IGRA PWV and spatial distance. All metrics are calculated using all match-ups.

Table 3 Statistics of the global evaluation of MERSI-II PWV in different PWV and distance ranges.

	Intervals	N	Slope	MB (cm)	MRB (%)	RMSE (cm)	CC
IGRA PWV (cm)	(0, 1]	15528	0.869	0.04	9.0	0.17	0.754
	(1, 2]	21698	0.878	-0.06	-3.7	0.26	0.709
	(2, 3]	11831	0.842	-0.19	-7.8	0.41	0.556
	(3, 4]	5493	0.867	-0.35	-10.1	0.57	0.483
	(4, 5]	2122	0.664	-0.55	-12.3	0.72	0.358
	>5	547	0.636	-0.94	-17.4	1.10	0.347
Spatial distance (km)	(0, 5]	31216	0.860	-0.08	-0.6	0.33	0.952
	(5, 10]	19972	0.844	-0.14	-3.4	0.38	0.953
	(10, 20]	4800	0.813	-0.19	-6.1	0.42	0.951
	>20	1231	0.792	-0.20	-5.9	0.47	0.933

Firstly, the IGRA PWV is binned and compared with~~comparison results between~~ the MERSI-II PWV. Most match-ups are located at the IGRA PWV interval ranging from 1.0 to 2.0 cm, and there are ~~the least~~not many samples above 5.0 cm. The MB and RMSE gradually increase with the increasing content of PWV, from 0.04 cm and 0.17 cm to -0.94 cm and 1.10 cm, respectively. ~~Besides~~Moreover, the fit-slope value is generally decreasing with the increasing content of PWV, and it can be concluded that there is an obvious underestimation when the PWV is larger than 5.0 cm. This result is similar to the conclusion drawn by Martins et al. (2019) in the evaluation of the PWV from MODIS, however, the slope is smaller. T~~t~~here is a good agreement between the IGRA PWV and MERSI-II PWV for dry conditions (<1.0 cm), with the highest CC value of 0.754. However, a slightly large discrepancy is observed in wet conditions (> 5.0cm). For MRB, there is a positive value of 9.0% in the 0.0–1.0 cm interval~~ of 0.0-1.0 cm~~, and this is also caused by the small PWV value. In contrast, all MRB is negative and the value of MRB~~ is~~ increas~~ing~~es with the content of PWV above 1.0 cm.

~~-and the IGRA PWV at different temporal intervals are shown in Figure 7. The MRB has significant differences at different temporal intervals. For MRB, the largest value of -3.73% appears under the condition with temporal discrepancy of 0-1 h, and the minimum value is -1.13% when the temporal discrepancy is 1-2 h. Moreover, the EE value varies obviously from 68.04% to 88.82%, and the value decreases with the increasing temporal discrepancy. RMSE changes from 0.23 cm to~~

~~0.36 cm with the increasing temporal discrepancy. PWVs from MERSI-II in all situations are highly correlated to the IGRA PWV with the CC values larger than 0.9320 in general, and they have the best correlation when the temporal discrepancy is less than 1 h. However, there is no noteworthy difference in different temporal intervals for MB. The MB with the temporal discrepancy of 1-2 h gets to the minimum at the value of -0.06 cm, and it is slightly different in other situations with values range from -0.07 cm to -0.10 cm. What's more, the slope of fitted line indicates that there is an obvious underestimation in the retrievals of PWV from MERSI-II, and the most underestimated PWV is in the condition of 4-6 h temporal discrepancy with the slope value of 0.826. When it is clear sky, there is a slight temporal variation of atmosphere water vapor, resulting in the unapparent differences at different temporal discrepancy intervals. Figure 7d shows the comparison with the temporal interval of 4-6 h. Obviously, there is a great number of points about half of all at this interval, and this is because the matchups are mostly located over East Asia and North America, where a temporal discrepancy of 4-6 h exists between the passing time of FY-3D and the release time of radiosonde.~~

~~Figure 7 Scatterplots of the PWV comparison between MERSI-II and IGRA at temporal intervals of (a) 0-1 h, (b)1-2 h, (c) 2-4 h and (d) 4-6 h.~~

~~Figure 8 presents t~~The results of ~~comparison between~~ the MERSI-II PWV and ~~the~~ IGRA PWV comparison in different distance intervals are also presented in ~~the t~~Table 3. Most points are located within the 0–5 km distance interval~~ of 0-5 km~~, and the number of points is ~~28756~~ 31,216 out of all ~~54214~~ 57,219 points. The MB increases with the extension of the distance between the IGRA station and the footprint of MERSI-II, and the largest MB is -0.~~15~~20 cm when the distance is ~~within the range of~~larger than 20~~-100~~ km. For the MRB, a more obvious difference is present within the 0–20 km distance range~~ of 0-20 km~~, as the value increases from -0.~~49~~6% to -~~5.93~~6.1% with the increasing distance. However, there is a slightly smaller MRB when the distance is larger than 20 km, and this probably has a relationship with the small number of samples. The RMSE has a ~~satisfied~~ value ranging from 0.33 cm to 0.47 cm~~,~~ and ~~is also~~ becomes~~ing~~ larger with the increasing distance. ~~In all distance intervals, the RMSE has a satisfied value within the range of 0.28-0.40 cm.~~ The large RMSE in the distance ~~condition of~~above 20~~-100~~ km is mainly caused by the obvious underestimation of MERSI-II PWV at some points. Overall, a good correlation exists between MERSI-II PWV and IGRA PWV with the CC value larger than 0.~~9060~~933~~, which is less than that in the effect of temporal discrepancy on evaluation. Besides, there are larger MB, MRB and RMSE in the evaluation of MERSI-II PWV with different distance discrepancy intervals. Consequently, the discrepancy of distance is a more influential factor than temporal discrepancy on the evaluation of PWV. Most points are located within the EE, and the EE value gets to decrease with the rise in distance and the value is all above 68.58%.~~

~~Figure 8 Scatterplots of the PWV comparison between MERSI-II and IGRA at the distance intervals of (a) 0-5 km, (b) 5-10 km, (c)10-20 km and (d) 20-100 km.~~

~~Table 2 illustrates the comparison results of the MERSI-II PWV in different intervals of altitude and latitude. Note that only the observations in April are selected in the comparison rather than the annual mean value (MEAN), and this is because averaging will smooth out the influence of altitude and latitude, which is highly related with the local climate situation, on the PWV retrievals. First, most observations are collected at low altitude below 200 m, and the MEAN of PWV is largest in the low altitude. The STD becomes smaller with the increase of altitude, which indicates that the PWV tends to be stabilized. There is a small slope of linear fit in the high altitude, so we make the conclusion that MERSI-II PWV has an underestimation, and the MB value alters from -0.08 cm to -0.02 cm for all altitudes. The largest MB appears in the sites with high altitude, and RMSE also has the largest value of 0.28 cm, and it is also found in the evaluation of AIRS PWV (Qin et al., 2012). This is because PWV is highly dependent on the altitude (Jiang et al., 2019), however, there is no height correction that can be used to eliminate false signals especially over complex terrain during the processing of MERSI-II PWV. The height correction is used in the validation of HY-2A PWV product and it is proved that can significantly reduce the RMSE from 0.50 cm to 0.21 cm, especially for the sites over 1000 m.~~

~~In addition, the EE value ranges from 71.04% to 79.42% at all altitudes, and it is least in high altitude sites. There are also larger MB and RMSE in the low altitude below 100 m, with the values are -0.07 cm and 0.28 cm, respectively. In the hazy conditions with high humidity over the low altitude sites, the uncertainty in the amount of haze is one of the largest error sources in the retrievals of PWV (Gao and Kaufman, 2003), however, the influence of haze is hardly corrected completely in the MERSI-II PWV retrieval algorithm. There is a high correlation between MERSI-II PWV and IGRA PWV, and the CC value is all above 0.8950. and the comparison of altitudes within 100-200 m presents a better performance.~~

~~The latitudinal distribution of PWV plays a key role in the study on the climatic change of global water vapor. Consequently, the latitude is divided in a step length of 15-20 degrees to analyze latitudinal performance of MERSI-II PWV product. Most of its samples are distributed from 20 °N to 50 °N, with the number of match-ups being totally 4249. The MEAN of PWV presents an obviously distribution opposite to latitude, with the largest value of 2.94 cm within 0°N -20°N. Meanwhile, the STD value in this region is also the largest, with the value of 1.01 cm. There also exists underestimation to the fit-slope value ranging from 0.716 to 0.860. Furthermore, the MB and MRB values are mostly negative as well, and the largest values of MB and MRB are within 0°N -20°N and 20°N -35°N, respectively. MERSI-II PWV has a great accuracy over high latitudes of the Southern Hemisphere, and the RMSE is less than 0.19 cm above the latitude of 35 °S. However, around the equator, the RMSE is large with the value greater than 0.43 cm. As discussed by Alraddawi et al (2018), for MODIS PWV, there are also noteworthy latitudinal decreases in MB, MRB and RMSE. With abundant water vapor around the equator, the cloud is easily formed and can micrify the PWV derived from MERSI-II because the MERSI-II can only measure the conditions above clouds. In addition, the temporal discrepancy can also lead to the bias because the discrepancy in the equatorial region is slight larger than in other regions overall.~~

~~Table 2 Summary statistics of MERSI-II PWV retrievals for different altitudes and latitudes in April.~~

	~~Intervals~~	~~N~~	~~MEAN (cm)~~	~~STD (cm)~~	~~Slope~~	~~MB (cm)~~	~~MRB (%)~~	~~RMSE (cm)~~	~~CC~~
~~Altitude (m)~~	~~[-50 100]~~	~~2593~~	~~1.24~~	~~0.79~~	~~0.828~~	~~-0.07~~	~~-1.25~~	~~0.28~~	~~0.9400~~
	~~[100 200]~~	~~1188~~	~~1.03~~	~~0.68~~	~~0.837~~	~~-0.02~~	~~2.38~~	~~0.22~~	~~0.9490~~
	~~[200 500]~~	~~1477~~	~~0.99~~	~~0.63~~	~~0.780~~	~~-0.06~~	~~-0.67~~	~~0.23~~	~~0.9460~~
	~~[500 2600]~~	~~1067~~	~~1.04~~	~~0.60~~	~~0.767~~	~~-0.08~~	~~-2.07~~	~~0.28~~	~~0.8950~~
~~Latitude (°N)~~	~~[-52 -35]~~	~~85~~	~~1.36~~	~~0.43~~	~~0.809~~	~~-0.07~~	~~-3.67~~	~~0.28~~	~~0.7990~~
	~~[-35 -20]~~	~~217~~	~~1.71~~	~~0.64~~	~~0.772~~	~~0.00~~	~~2.67~~	~~0.36~~	~~0.8300~~
	~~[-20 0]~~	~~67~~	~~2.66~~	~~0.90~~	~~0.716~~	~~-0.13~~	~~-2.12~~	~~0.43~~	~~0.8890~~
	~~[0 20]~~	~~140~~	~~2.94~~	~~1.01~~	~~0.764~~	~~-0.20~~	~~-3.89~~	~~0.54~~	~~0.8670~~
	~~[20 35]~~	~~1226~~	~~1.59~~	~~0.82~~	~~0.729~~	~~-0.16~~	~~-5.22~~	~~0.39~~	~~0.9040~~
	~~[35 50]~~	~~3023~~	~~0.93~~	~~0.45~~	~~0.771~~	~~-0.05~~	~~-0.05~~	~~0.19~~	~~0.9150~~
	~~[50 60]~~	~~1467~~	~~0.76~~	~~0.35~~	~~0.860~~	~~0.00~~	~~1.89~~	~~0.13~~	~~0.9270~~
	~~[60 76]~~	~~100~~	~~0.64~~	~~0.28~~	~~0.838~~	~~0.00~~	~~2.97~~	~~0.11~~	~~0.9250~~

~~5 Application of PWV product in Qinghai-Tibet Plateau~~

~~The Qinghai-Tibet Plateau (QTP) plays an important role in regional weather and climate, especially for East Asia. As we all know, water vapor can significantly affect climate change, radiation balance and hydrological cycle. Thus, studying for the atmospheric water vapor distribution over QTP is useful to understand the influence of QTP on the weather and climate. However, the ground-based observations of PWV are sparse and unevenly distributed, so it is difficult to investigate the~~

~~distribution of PWV over QTP with ground-based observations. Satellite-based measurement has been widely used in the analysis on the distribution of PWV over QTP owing to its advantage of large area coverage. In this section, the seasonal variation and distribution of PWV over TP are analyzed with the MERSI-II measurements from September 2018 to June 2021.~~

~~Figure 9 (a, b) show the distribution of PWV over QTP during the warm (April to September) and cold (October to March) seasons. The PWV shows a distribution consistent with altitude, and there is high PWV in low altitude but small PWV in high altitude. The large PWV is centered in the Bay of Bengal, with values above 4.0 cm and 2.0 cm in warm and cold seasons, respectively. The small PWV is mainly located over the western part of Tibet and it is more significant in cold season with a large area having the PWV less than 0.5 cm. Around the Brahmaputra River, which is a precipitation center over QTP, an obvious water vapor transport path lies along the Brahmaputra Grand Canyon. The water vapor from the Bay of Bengal region is transported into QTP through this path, making a higher PWV in this area. Therefore, a comparison between the two stations of Motuo and Shimian is analyzed to shed light on the role of the Brahmaputra Grand Canyon in the transport of water vapor. The two stations, Motuo and Shimian, are situated at similar latitudes but different longitudes (Figure 9c). It is noted that the altitude of Motuo station is 1279.0 m, higher than the altitude of Shimian station (875.1 m). Figure 9d shows the annual variation of PWV at both sites represented as box diagrams, which are defined as follows: bottom and top of boxes denote the 25th and 75th percentiles with the horizontal lines inside the box being the median. The dotted lines represent the range of the adjacent value, which is the most extreme value that is not an outlier, and the outliers are marked by crosses (Zhang et al., 2020). As we have discussed above, it is reasonable that large PWV should be found in a low altitude generally. However, the trends of PWV at the two sites are similar, and there are nearly identical PWV mean values for both sites. Besides, the annual variation of PWV shows that the PWV of Motuo site is obviously higher than that of Shimian in July, which means that the PWV transport of the Brahmaputra Grand Canyon is more significant at this moment.~~

~~Figure 9 The distribution of PWV over QTP in (a) warm and (b) cold seasons. (c) Map illustrating the Motuo and Shimian stations. (d) Statistics of PWV at Motuo (red line) and Shimian (blue line) stations represented as box diagrams. Bottom and top of boxes denote the 25th and 75th percentiles, with the horizontal lines inside the box being the median value; the dotted lines represent the range of the adjacent value, which is the most extreme value that is not an outlier; the outliers are marked by crosses. The lines are the mean seasonal PWV.~~.

~~6~~ 5 Summary and Conclusions

In this paper, we ~~have~~ evaluated the global PWV product derived from FY-3D/MERSI-II by ~~comparison~~ comparing ~~to~~ with the PWV from 462~~626~~ IGRA stations, with ~~54214~~ 57,219 match-up~~ point~~s during the period from September 2018 to

June 2021. ~~There is a good agreement between the average PWVs from FY-3D/MERSI-II and IGRA, but the FY-3D/MERSI-II PWV is slightly underestimated.~~ The monthly averaged PWV derived from MERSI-II shows a distribution of decreasing values with an increasing latitude. ~~The averaged PWV from MERSI-II and IGRA both are presented as the distribution opposite to latitude, and generally featured with one low center over the east of Russia and the northeast of China, and two high PWV areas concentrated in the surrounding areas of the Bay of Bengal and the central part of South America.~~

Overall, PWVs derived from MERSI-II and IGRA ~~have a~~are in good agreement with the CC value of 0.~~9400~~951. However, there is a slight underestimation for the FY-3D/MERSI-II PWV, and ~~The~~ the values of MB and MRB are -0.~~09~~ 11 cm and -~~1.90~~2.2%, respectively, while the RMSE is 0.~~31~~ 36 cm ~~with a satisfactory EE value of 75.36%~~. The h~~H~~istogram~~s~~ of MB ~~and MRB~~ indicates that ~~the values of~~ MB value ~~and MRB both~~ approaches zero and mostly distributes between -1.00 cm and 0.50 cm~~, however, the distribution patterns are~~ ~~is~~ with a left-skewed distribution pattern ~~and right-skewed, respectively~~. ~~The peak values of MB and MRB are 0.00 cm and -2.38%, with STDs are 0.25 cm and 16.8%.~~

For all sites, the MB value is low and ~~80% of the~~most sites have ~~the~~ a value~~s~~ between -0.~~28~~ 41 cm and 0.05 cm. In the west and south of Asia, the MERSI-II PWV is obviously underestimated with an MB value larger than -0.41 cm. However, the overestimated PWV are mostly distributed in the surrounding areas of the Black Sea and ~~the middle part of~~central South America. Large MRB values are mostly l~~ie~~ocate~~s~~d in eastern Russia, northeastern China, and central South America. Most sites have a small RMSE~~90% of all sites have low RMSE values~~ below 0.~~49~~ 48 cm, ~~-~~and CC values above 0.~~8213~~873. Lastly, it is observed that there are large MB and RMSE values while there are small CC values around the equator, especially in South and Southeast Asia.

The MERSI-II PWV is in good agreement with the PWV obtained from IGRA with all CC values larger than 0.921. There is a slight underestimation of MERSI-II PWV for all seasons with an MB value below -0.18 cm, and it is significant in the summer. In addition, the MRB and RMSE also have the largest magnitude in summer. The underestimation of PWV in summer is probably due to the presence of thin clouds, which weaken the radiation signal observed by the satellite. We found the MRB with a positive value in the winter, and this is mainly due to the low PWV then. For RMSE, there is a larger value in the Southern Hemisphere and the greatest RMSE value is 0.49 cm in summer.

~~In winter, the values of MB and RMSE are the lowest, being -0.04 cm and 0.27 cm, respectively. For MRB, it has maximum value in summer but minimum value in spring, and apart from that, the MRB is positive in winter due to the small PWV with a high positive MB in winter. The CC value is larger than 0.9080 in all four seasons and the EE value varies from 73.10% to 77.47%. There is a significant monthly variation in the evaluation of MERSI-II PWV product. The peak MBs are in February and July over the Southern and Northern Hemisphere, respectively. The largest RMSE is 0.40 cm in December in Southern Hemisphere. Besides, there is a better correlation between PWVs derived from MERSI-II and IGRA in Southern Hemisphere, and all CC values are larger than 0.9070 except in July. The EE values during all months are larger than 66%, indicating that there is a satisfactory coherence between the PWVs from MERSI-II and IGRA.~~

In addition, the ~~influence~~ influencing factors on the evaluation are also discussed. First of all, there is an obvious effect of binned IGRA PWV on the evaluation, and in general, the MB and RMSE are both increasing with the IGRA PWV. In the dry condition (<1.0 cm), there is a positive MRB value of 9.0%, and this is also mainly due to the low PWV value. Nevertheless, the MRB is all negative and increases with an IGRA PWV above 2.0 cm. ~~the influence of temporal discrepancy between the passing time of FY-3D and the release time of radiosonde is analyzed. There are some differences within different temporal intervals. MRB has the largest value with temporal discrepancy of 0-1 h and the minimum value is found when the temporal discrepancy is 1-2 h. EE value declines with the ascending temporal discrepancy from 68.04% to 88.82%. However, there is no noteworthy difference in MB within different temporal intervals and the MB value changes from -0.06 cm to -0.10 cm. For RMSE, the greatest value is 0.36 cm, seen at the temporal discrepancy of 4-6 h. All of CC values are larger than 0.9320 and the best correlation is found when the temporal discrepancy is less than 1 h.~~ Subsequently, the evaluations within different distance intervals are presented in order to reveal the effect of distance between the footprint of ~~FY-3D~~the satellite and ~~radiosonde~~ the IGRA site~~s~~ location. The MB varies positively with ~~the growth of the~~the increasing distance, and the largest MB is -0.~~15~~ 20 cm within the distance ~~of~~ above 20~~-100~~ km. The MRB ~~is increasing~~ increases from -0.~~49~~6% to -~~5.93~~6.1% with the distance increases~~ing~~ ~~distance~~from 0 to 20 km. The RMSE also increases with the distance increased and the large RMSE is mainly caused by the obvious underestimation of MERSI-II PWV at some points with the spatial distance larger than 20 km. ~~However, the CC value is less than that in different temporal intervals, besides, there are larger MB, MRB and RMSE in the evaluation of MERSI-II PWV with different distance discrepancy intervals, and this can be concluded as the discrepancy of distance has more effect on the evaluation of PWV than temporal discrepancy. In general, large MB and RMSE are both distributed at the high-altitude stations, with the values of -0.08 cm and 0.28 cm, and the STD becomes smaller with the increase of altitude. However, the least EE value is found in high altitude sites. From the analysis of latitudinal performance of MERSI-II PWV, the MEAN of PWV shows a distribution opposite to latitude. The largest values of MB and MRB are within 0°N -20°N and 20°N -35°N, respectively. The RMSE is less than 0.19 cm above the latitude of 35 °S, however, the RMSE has large value around the equator with the value greater than 0.43 cm.~~

The global evaluation of the MERSI-II PWV product can explore a wide variety of applications of this product, and the analysis of the influencing factors on the evaluation can be helpful for improving the PWV retrieval algorithm. Although we have partially explained the underestimation of the PWV from MERSI-II, other influencing factors, such as the solar zenith angle, the precision of the transmittance calculation and the uncertainty of the radiation signals should be studied in the future. Furthermore, how to quantitate the influence of aerosols (e.g., dust, haze) and thin cirrus clouds on the PWV retrieval is also a key problem that should be explored in the application of the PWV product.

~~Finally, the PWV product derived from MERSI-II is employed to analyze the PWV distribution over QTP. In Both warm and cold seasons, the large PWV is concentrated in the Bay of Bengal, and the values are above 4.0 cm and 2.0 cm, respectively. As the distribution of PWV shows in clear sky condition, the water vapor transport path along the Brahmaputra Grand Canyon~~

~~is obviously with a large PWV. What's more, the comparison between the monthly variations of PWV at Motuo and Shimian sites suggests that the two stations both enjoy the nearly identical PWV mean values. In terms of the altitudes of the two stations, the results indicate that the Brahmaputra Grand Canyon plays a key role in the transport of water vapor, especially in July.~~

Data availability

The MERSI-II PWV product is available from http://satellite.nsmc.org.cn/PortalSite/Data/Satellite.aspx, the IGRA data is available from ftp://ftp.ncdc.noaa.gov/pub/data/igra, and the global AERONET data are provided at https://aeronet.gsfc.nasa.gov. The altitude data set is provided by Geospatial Data Cloud site, Computer Network Information Center, Chinese Academy of Sciences at http://www.gscloud.cn. The processed data are available from Zenodo (https://doi.org/10.5281/zenodo.5563205~~10.5281/zenodo.5105083~~).

Author contributions

Conceptualization, ZWG and WL; data curation, WL, YY and HQX; formal analysis, ZWG, YY and XGR; writing-original draft preparation, ZWG; writing-review and editing, ZWG and WL; supervision, XGR and HXQ; funding acquisition, XGR and CCG. All authors have reviewed and agreed on the final version of the manuscript.

Competing interests

The authors declare that they have no conflict of interest.

Acknowledgments

This work is supported by The Second Tibetan Plateau Scientific Expedition and Research (STEP) program (Grant No. 2019QZKK0105); National Natural Science Foundation of China (NSFC) under Grant No. 41705019 and 41620104009; the Hubei Meteorological Bureau project under Grant No. 2018Q04; and NSFC under Grant No. 91637211.We appreciate the National Satellite Metrological Center of China Meteorological Administration (CMA) for providing the MERSI-II PWV product, the National Climatic Data Center (NCDC) for providing IGRA data, and the principal investigators and their staff for establishing and maintaining the AERONET sites used in this study. The altitude data set is provided by Geospatial Data Cloud site, Computer Network Information Center, Chinese Academy of Sciences.

References

Adeyemi, B. and Schulz, J.: Analysis of water vapor over nigeria using radiosonde and satellite data, J. Appl. Meteor. Climatol, 51, 1855-1866, https://doi.org/10.1175/JAMC-D-11-0119.1, 2012.

Alexandrov, M. D., Schmid, B., Turner, D. D., Cairns, B., Oinas, V., Lacis, A.A., Gutman S. I., Westwater, E. R. Smirnov, A., and Eilers J.: Columnar water vapor retrievals from multifilter rotating shadow band radiometer data, J. Geophys. Res. Atmos., 114, D02306, https://doi.org/10.1029/2008JD010543, 2009.

Alraddawi, D., Sarkissian, A., Keckhut, P., Bock, O., Noël, S., and Bekki, S.: Comparison of total water vapour content in the Arctic derived from GNSS, AIRS, MODIS and SCIAMACHY, Atmos. Meas. Tech., 11(5), 2949-2965, https://doi.org/10.5194/amt-11-2949-2018, 2018.

Antón, M., Loyola, D., Román, R., and Vömel, H.: Validation of GOME-2/MetOp-A total water vapour column using reference radiosonde data from the GRUAN network, Atmos. Meas. Tech., 8, 1135-1145, https://doi.org/10.5194/amt-8-1135-2015, 2015.

Bennartz, R., and Fischer, J.: Retrieval of columnar water vapour over land from back-scattered solar radiation using the Medium Resolution Imaging Spectrometer (MERIS), Remote Sens. Environ., 78(3), 274-283, https://doi.org/10.1016/S0034-4257(01)00218-8, 2001.

Bevis, M., Businger, S., Herring, T. A., Rocken, C., Anthes, R. A., and Ware, R. H.: GPS meteorology: Remote sensing of atmospheric water vapor using the Global Positioning System, J. Geophys. Res. Atmos., 97(D14), 15787-15801, https://doi.org/10.1029/92JD01517, 1992.

Boukabara, S., Garrett, K., and Chen, W.: Global Coverage of Total Precipitable Water Using a Microwave Variational Algorithm, IEEE T. Geosci. Remote, 48, 3608-3621, https://doi.org/10.1109/TGRS.2010.2048035, 2010.

Che, H. Z., Gui, K., Chen, Q. L., Zheng, Y., Yu, J., Sun, T. Z., Zhang, X. Y., and Shi, G. Y.: Calibration of the 936 nm water-vapor channel for the China aerosol remote sensing NETwork (CARSNET) and the effect of the retrieval water-vapor on aerosol optical property over Beijing, China, Atmos. Pollut. Res., 7(5), 743-753, https://doi.org/10.1016/j.apr.2016.04.003, 2016.

Chen, B. and Liu, Z.: Global water vapor variability and trend from the latest 36 year (1979 to 2014) data of ECMWF and NCEP reanalyses, radiosonde, GPS, and microwave satellite, J. Geophys. Res. Atmos.,121,11442-11462, https://doi.org/10.1002/2016JD024917, 2016.

Dessler, A.E. and Wong, S.: Estimates of the water vapor climate feedback during El Niño–Southern Oscillation, J. Climate, 22(23), 6404-6412, https://doi.org/10.1175/2009JCLI3052.1, 2009.

Durre, I., Williams Jr., C. N., Yin, X. G., and Vose, R. S.: Radiosonde-based trends in precipitable water over the Northern Hemisphere: An update, J. Geophys. Res. Atmos., 114, D05112, https://doi.org/10.1029/2008JD010989, 2009.

Durre, I., Yin, X., Vose, R. S., Applequist, S., and Arnfield, J.: Enhancing the Data Coverage in the Integrated Global Radiosonde Archive, J. Atmos. Ocean. Tech., 35(9), 1753-1770, https://doi.org/10.1175/JTECH-D-17-0223.1, 2018.

Gao, B. C. and Kaufman, Y. J.: Water vapor retrievals using Moderate Resolution Imaging Spectroradiometer (MODIS) near-infrared channels, J. Geophys. Res. Atmos., 108, D13, https://doi.org/10.1029/2002JD003023, 2003.

Held, I. M. and Soden, B. J.: Water vapor feedback and global warming, Annu. Rev. Energy Environ., 25, 441-475, https://doi.org/10.1146/annurev.energy.25.1.441, 2000.

Holben, B. N., Eck, T. F., Slutsker, I., Tanré, D., Buis, J. P., Setzer, A., Vermote, E., Reagan, J.A., Kaufman, Y.J., Nakajima, T., Lavenu, F., Jankowiak, I., and Smirnov, A.: AERONET—A federated instrument network and data archive for aerosol characterization, Remote Sens. Environ., 66(1), 1-16, https://doi.org/10.1016/S0034-4257(98)00031-5, 1998.

~~Jiang, J., Zhou, T., and Zhang, W.: Evaluation of satellite and reanalysis precipitable water vapor data sets against radiosonde observations in central Asia, Earth Space Sci., 6, https://doi.org/10.1029/2019EA000654, 2019.~~

Kiehl, J. T. and Trenberth, K. E.: Earth's annual global mean energy budget, B. Am. Meteorol. Soc., 78, 197-208, https://doi.org/10.1175/1520-0477(1997)078%3C0197:EAGMEB%3E2.0.CO;2, 1997.

~~Levy, R. C., Remer, L. A., Kleidman, R. G., Mattoo, S., Ichoku, C., Kahn, R., and Eck, T. F.: Global evaluation of the Collection 5 MODIS dark-target aerosol products over land, Atmos. Chem. Phys., 10(21), 10399-10420, https://doi.org/10.5194/acp-10-10399-2010, 2010.~~

Li, Z. H., Muller, J. P., Cross, P., Albert, P., Hewison, T., Watson, R., Fischer, J., and Bennartz, R.: Validation of MERIS near IR water vapour retrievals using MWR and GPS measurements, MERIS user workshop, ESA ESRIN, Frascati, Italy, 10-13 Nov 2003, 2003.

Liu, H. L., Tang, S. H., Zhang, S. L., and Hu, J. Y.: Evaluation of MODIS water vapour products over China using radiosonde data, Int. J. Remote Sens., 36(2), 680-690, https://doi.org/10.1080/01431161.2014.999884, 2015.

Liu, J. M., Liang, H., Sun, Z. A., and Zhou, X. J.: Validation of the Moderate-Resolution Imaging Spectroradiometer precipitable water vapor product using measurements from GPS on the Tibetan Plateau, J. Geophys. Res. Atmos., 111, D14103, https://doi.org/10.1029/2005JD007028, 2006.

Liu, Z. Z., Wong, M. S., Nichola, J. and Chan, P. W.: A multi-sensor study of water vapour from radiosonde, MODIS and AERONET: a case study of Hong Kong, Int. J. Climatol., 33, 109-120, https://doi.org/10.1002/joc.3412, 2013.

Lu, N.: Biases and abrupt shifts of monthly precipitable water from Terra MODIS, Remote Sens., 11(11), 1315. https://doi.org/10.3390/rs11111315, 2019.

Lu, N., Qin, J., Yang, K., Gao, Y., Xu, X. D., and Koike, T.: On the use of GPS measurements for Moderate Resolution Imaging Spectrometer precipitable water vapor evaluation over southern Tibet, J. Geophys. Res. Atmos., 116, D23117, https://doi.org/10.1029/2011JD016160, 2011.

Malderen, R. V., Brenot, H., Pottiaux, E., Beirle, S., Hermans, C., Mazière, M. D., Wagner, T., Backer, H. D., and Bruyninx, C.: A multi-site intercomparison of integrated water vapour observations for climate change analysis, Atmos. Meas. Tech., 7, 2487-2512, https://doi.org/10.5194/amt-7-2487-2014, 2014.

Martins, V. S., Lyapustin A., Wang, Y. J., Giles, D. M., Smirnov, A., Slutsker, I., and Korkin S. Global validation of columnar water vapor derived from EOS MODIS-MAIAC algorithm against the ground-based AERONET observations, Atmos. Res., 225, 181-192, https://doi.org/10.1016/j.atmosres.2019.04.005, 2019.

Meng, X. C., Cheng, J. and Liang, S. L.: Estimating land surface temperature from Feng Yun-3C/MERSI data using a new land surface emissivity scheme, Remote Sens., 9(12), 1247, https://doi.org/10.3390/rs9121247, 2017.

Naumann, A. K. and Kiemle, C.: The vertical structure and spatial variability of lower-tropospheric water vapor and clouds in the trades, Atmos. Chem. Phys., 20, 6129-6145, https://doi.org/10.5194/acp-20-6129-2020, 2020.

Niilo, K., Jukka, K., Viktoria, S., Johanna, T., Margherita, G., and Pieter, V.: Validation of GOME-2/Metop total column water vapour with ground-based and in situ measurements, Atmos. Meas. Tech., 9, 1533-1544, https://doi.org/10.5194/amt-9-1533-2016, 2016.

Pérez-Ramírez, D., Whiteman, D. N., Smirnov, A., Lyamani, H., Holben, B. N., Pinker, R., Andrade, M., and Alados-Arboledas, L.: Evaluation of AERONET precipitable water vapor versus microwave radiometry, GPS, and radiosondes at ARM site, J. Geophys. Res. Atmos., 119, 9596-9613, https://doi.org/10.1002/2014JD021730, 2014.

Pérez-Ramírez, D., Smirnov, A., Pinker, R. T., Petrenko, M., Román, R., Chen, W., Ichoku, C., Noël, S., Abad, G. G., Lyamani, H., and Holben, B. N.: Precipitable water vapor over oceans from the Maritime Aerosol Network: Evaluation of global models and satellite products under clear sky conditions, Atmos. Res., 215, 294-304, https://doi.org/10.1016/j.atmosres.2018.09.007, 2019.

Prasad, A. K. and Singh, R. P.: Validation of MODIS Terra, AIRS, NCEP/DOE AMIP-II Reanalysis-2, and AERONET Sun photometer derived integrated precipitable water vapor using ground-based GPS receivers over India, J. Geophys. Res. Atmos., 114, D05107, https://doi.org/10.1029/2008JD011230, 2009.

Qin, J., Yang, K., Koike, T., Lu, H., Ma, Y. M. and Xu, X. D.: Evaluation of AIRS precipitable water vapor against ground-based GPS measurements over the Tibetan Plateau and its surroundings, J. Meteorol. Soc. Jpn., 90, 87-98, https://doi.org/10.2151/jmsj.2012-C06, 2012.

Rakesh, V., Randhir, S., Pal, P. K., and Joshi, P. C.: Impacts of satellite-observed winds and total precipitable water on WRF short-range forecasts over the Indian region during the 2006 summer monsoon, Wea. Forecasting, 24, 1706-1731, https://doi.org/10.1175/2009WAF2222242.1, 2009.

Sobrino, J. A., Juan, C. J., Cristian, M. and Guillem, S.: Evaluation of Terra/MODIS atmospheric profiles product (MOD07) over the Iberian Peninsula: a comparison with radiosonde stations, Int. J. Digit. Earth, 8(10), 1-13, https://doi.org/10.1080/17538947.2014.936973, 2014.

Solbrig, J. E.: Thin cloud length scales using CALIPSO and CloudSat data, M.S. thesis, Department of Atmospheric Sciences, Texas A&M University, Texas, U.S.A, 62 pp., 2009.

Trenberth, K. E., Dai, A. G., Rasmussen, R. M., and Parsons, D. B.: The changing character of precipitation, B. Am. Meteorol. Soc., 84(9), 1205-1218, https://doi.org/10.1175/BAMS-84-9-1205, 2003.

Turner, D. D., Lesht, B. M., Clough, S. A., Liljegren, J. C., Revercomb, H. E., and Tobin, D. C.: Dry Bias and Variability in Vaisala RS80-H Radiosondes: The ARM Experience, J. Atmos. Ocean. Tech., 20, 117-132, https://doi.org/10.1175/1520-0426(2003)020<0117:DBAVIV>2.0.CO;2, 2003.

Wang, L., Hu, X. Q., Xu, N., and Chen, L. Water vapor retrievals from near-infrared channels of the advanced Medium Resolution Spectral Imager instrument onboard the Fengyun-3D satellite, Adv. Atmos. Sci., https://doi.org/10.1007/s00376-020-0174-8, 2021.

Wang, J. H., Dai, A. G., and Mears, C.: Global water vapor trend from1988 to 2011 and its diurnal asymmetry based on GPS, radiosonde, and microwave satellite measurements, J. Climate, 29(14), 5205-5222. https://doi.org/10.1175/JCLI-D-15-0485.1, 2016.

Wang, J. H., Zhang, L. Y., Dai, A. G., Hove, T. V., and Baelen, J. V.: A near-global, 2-hourly data set of atmospheric precipitable water from ground-based GPS measurements, J. Geophys. Res. Atmos., 112, D11107. https://doi.org/10.1029/2006JD007529, 2007.

Wang, S. M., Xu, T. H., Nie, W. F., Jiang, C. H., Yang, Y. G., Fang, Z. L., Li M. W., and Zhang Z.: Evaluation of precipitable water vapor from five reanalysis products with ground-based GNSS observations, Remote Sens., 12(11), 1817, https://doi.org/10.3390/rs12111817, 2020.

Westwater, E. R.: The accuracy of water vapor and cloud liquid determination by dual-frequency ground-based microwave radiometry, Radio Sci., 13(4), 677-685, https://doi.org/10.1029/RS013i004p00677, 1978.

Wu, R. H., Zhang, P., Xu, N., Hu, X. Q., Chen, L., Zhang, L., and Yang, Z. D.: FY-3D MERSI on-orbit radiometric calibration from the lunar view, Sensors, 20(17), 4690, https://doi.org/10.3390/s20174690, 2020a.

Wu, Z., Liu, Y., Liu, Y., Wang, J., He, X., Xu, W., Ge, M., and Schuh, H.: Validating HY-2A CMR precipitable water vapor using ground-based and shipborne GNSS observations, Atmos. Meas. Tech., 13, 4963–4972, https://doi.org/10.5194/amt-13-4963-2020, 2020b.

Xu, N., Niu, X. H., Hu, X. Q., Wang, X. H., Wu, R. H., Chen, S. S., Chen, L., Sun L., Ding L., Yang Z. D., and Zhang, P.: Prelaunch calibration and radiometric performance of the advanced MERSI II on FengYun-3D, IEEE T. Geosci. Remote, 56, 4866-4875, https://doi.org/10.1109/TGRS.2018.2841827, 2018.

Yang, Z. D., Zhang, P, Gu, S. Y.,Hu, X. Q.,Tang, S. H.,Yang, L. K., Xu, N., Zhen, Z. J., Wang L., Wu, Q., Dou, F. L., Liu, R. X., Wu, X., Zhu, L., Zhang, L. Y., Wang, S. J., Sun, Y Q., and Bai, W. H.: Capability of Fengyun-3D satellite in earth system observation, J. Meteorol. Res-PRC., 33(6), 1113-1130, https://doi.org/10.1007/s13351-019-9063-4, 2019.

Zhao, T. B., Dai, A. G., and Wang, J. H.: Trends in tropo-spheric humidity from 1970 to 2008 over China from a homogenized radiosonde dataset, J. Climate, 25, 4549-4567, https://doi.org/10.1175/jcli-d-11-00557.1., 2012.

Zhang, F. Z., Barriot, J.-P., Xu, G. C., and Yeh, T.-K.: Metrology assessment of the accuracy of precipitable water vapor estimates from GPS data acquisition in tropical areas: the Tahiti case, Remote Sens., 10 (5), 758, https://doi.org/10.3390/rs10050758, 2018.

Zhang, J. Q., Chen, H. B., Li, Z. Q., Fan, X. H., Peng, L., Yu, Y., and Cribb, M.: Analysis of cloud layer structure in Shouxian, China using RS92 radiosonde aided by 95 GHz cloud radar, J. Geophys. Res. Atmos., 115, D00K30, https://doi.org/10.1029/2010JD014030, 2010.

Zhang, W. G., Xu, G. R., Wan, R., He, W. H., and Feng, G. L.: Analysis of the characteristic of liquid water and water vapor detected by ground-based microwave radiometer, Torrential Rain and Disasters, 34 (4), 367-374, 2015. (in Chinese with English abstract)~~Zhang, W. G., Xu, G. R., Xi, B. K., Ren, J., Wan, X., Zhou, L. L., Cui C. G., and Wu, D. Q.: Comparative study of cloud liquid water and rain liquid water obtained from microwave radiometer and micro rain radar observations over central China during the monsoon, J. Geophys. Res. Atmos., 125, e2020JD032456, https://doi.org/10.1029/2020JD032456, 2020.~~